Remote Controlled Optical Manipulation of Bimetallic Nanoparticle Catalysts using Peptides

Received 00th January 20xx,
Accepted 00th January 20xx

DOI: 10.1039/x0xx00000x

Randy L. Lawrence,[a,‡] Mary O. Olagunju,[a,‡] Yang Liu,[b] Krishnamurthy Mahalingam,[c] Joseph M. Slocik,[c] Rajesh R. Naik,[c] Anatoly I. Frenkel,[b,d]* Marc R. Knecht, [a,e,]*

Bimetallic nanoparticles remain a promising avenue to achieve highly reactive catalysts. In this contribution, we demonstrate the use of a photoswitchable peptide for the production of PdAu bimetallic nanoparticles at a variety of Pd:Au ratios. Using this peptide, the biomolecular overlayer structure can be switched between two different conformations (*cis vs. trans*) via light irradiation, thus accessing two different surface structures. The composition and arrangement of the materials was fully characterized, including atomic-level analyses, after which the reactivity of the bimetallic materials was explored using the reduction of 4-nitrophenol as a model system. Using these materials, it was demonstrated that the reactivity was maximized for the particles prepared at a Pd:Au ratio of 1:3 and with the peptide in the *cis* conformation. Such results present routes to a new generation of catalysts that could be remotely activated for on/off reactivity as a function of the ligand overlayer conformation.

Introduction

Catalytic nanoparticles (NPs) have been employed for numerous chemical reactions, including heterogeneous and pseudo-homogeneous systems.[1, 2] Notably, monometallic NPs can catalyze a variety of reactions ranging from olefin hydrogenation[3-6] and CO oxidation,[7, 8] to C-C coupling reactions.[9, 10] The efficient reactivity of metal NPs is typically attributed to their small size, leading to a high surface to volume ratio that maximizes metal exposure. While changes in reactivity are anticipated from monometallic NPs based upon the metal identity, enhanced reactivity can be achieved when multiple metals are incorporated into a single material.[10-14] For instance, bimetallic NPs produced using Pd and Au have demonstrated enhanced reactivity as compared to their monometallic counterparts.[11, 15-17] This effect can be explained by two factors: electronic changes in the NP and the geometric arrangement of atoms within the material. For PdAu specifically, the more electronegative Au pulls electron density from the Pd, thus changing the electronic structure of the material, leading to enhanced reactivity for the bimetallic NPs.

While the catalytic reactivity is typically driven by the metallic component, for unsupported NPs, ligands must be present on the particle surface to prevent material aggregation.[18] A variety of different ligands have been employed ranging from organic to biological molecules.[18, 19] In most cases, the ligands employed are largely static and covalently bound, thus producing a rigid overlayer that diminishes reactivity by hindering access to the surface active sites. Recently, we have demonstrated that peptide-based ligands are capable of generating a dynamic overlayer that can reversibly reconfigure between two different conformations using light as a trigger.[20, 21] As such, this alters surface accessibility between the two ligand configurations, resulting in altered reactivity.[22-24] To achieve peptide reconfiguration, a photoswitch was integrated into a materials binding sequence, where optical switching between the *cis* and *trans* conformation of the photoswitch led to changes in the peptide overlayer structure on the NP surface. This was previously demonstrated using monometallic Au, Ag, and Pd NPs passivated with a peptide-photoswitch hybrid, giving rise to altered material reactivity as a function of the metal composition, peptide overlayer conformation (e.g. *trans* or *cis*), and the position of the photoswitch within the peptide sequence.[22-24]

Herein, the generation of catalytically reactive bimetallic PdAu NPs with a dynamic, optically responsive biological ligand layer was investigated and compared to the previously reported monometallic counterparts. The peptide-photoswitch hybrid was achieved through the conjugation of the AuBP1 peptide (WAGAKRLVLRRE), previously identified with affinity for Au,[25] with an azobenzene-based photoswitch moiety.[26] Using this

---

[a] *Department of Chemistry, University of Miami, 1301 Memorial Drive, Coral Gables, Florida 33146, USA.*
[b] *Department of Materials Science and Chemical Engineering, Stony Brook University, Stony Brook, New York 11794, USA.*
[c] *Air Force Research Laboratory, Wright-Patterson Air Force Base, Ohio 45433, USA.*
[d] *Chemistry Division, Brookhaven National Laboratory, Upton, New York 11973, USA.*
[e] *Dr. J.T. Macdonald Foundation Biomedical Nanotechnology Institute, university of Miami, UM Life Science Technology Building, 1951 NW 7th Ave, Suite 475, Miami, Florida 33136, USA.*

[‡] *These authors contributed equally.*

Electronic Supplementary Information (ESI) available: additional XAFS analysis and catalytic results. See DOI: 10.1039/x0xx00000x hybrid, the preparation of PdAu bimetallic NPs was investigated that varied the Pd:Au ratio. Each system was fully characterized using UV-vis spectroscopy, transmission electron microscopy (TEM), X-ray absorption fine structure spectroscopy (XAFS), and inductively coupled plasma mass spectometery (ICP-MS). These results demonstrated that the system generated bimetallic NPs where the two metals were fully alloyed together. After assessing the dynamic reconfiguration of the peptide overlayer, the catalytic capacity was probed via the reduction of 4-nitrophenol. From the catalytic studies, it was evident that changes in the reactivity were present as a function of both the bioligand overlayer structure (*cis vs. trans*) and the underlying bimetallic composition. In this regard, the greatest degree of reactivity was observed from the PdAu NPs prepared at a 1:3 Pd:Au ratio, while greater reactivity was generally observed for the materials with the peptide overlayer in the *cis* conformation. These results demonstrate two key factors: 1. The AuBP1 peptide possess inherent affinity to stabilize a wide composition of noble metal materials (advancing to bimetallic compositions), while allowing for dynamic overlayer reconfiguration, and 2. Peptide-based approaches can be employed to control the reactivity of bimetallic NPs. From these studies, routes to potentially achieving on/off reactivity through careful selection of metal composition, bimetallic ratio, peptide sequence, and photoswitch position could be possible.

Experimental

Materials

Trifluoroacetic acid (TFA), 4-nitrophenol (4-NP), and tri-isopropyl silane were purchased from Alfa Aesar, while K_2PdCl_4 and $HAuCl_4$ were purchased from Strem Chemicals, Inc. and Acros Organics, respectively. $NaBH_4$ was procured from Millipore-Sigma. Methanol, acetonitrile, and *N,N*-dimethylformamide (DMF) were sourced from BDH. Lastly, piperidine, *N,N*-diisopropylethylamine, *N,N,N′,N′*-tetramethyl-O-(1H-benzotriazol-1-yl)uranium hexafluorophosphate, hydroxybenzotriazole, Wang resins, and fluorenylmethyloxycarbonyl (Fmoc)-protected amino acids were purchased from Advanced Chemtech. All experiments were carried out with ultrapure water (Millipore, 18.2 MΩ cm), and all reagents were used without additional purification.

Peptide Synthesis

Automated peptide synthesis using standard solid-phase Fmoc protocols was employed on a TETRAS peptide synthesizer (Creosalus). The peptides were cleaved from the resin with a 90:3:5:2 mixture of TFA/ethanedithiol/thioanisole/anisole for 4 h, and purification was achieved through reverse phase HPLC (Waters Co. Delta 600 with 2498 UV-vis detector). The purified peptide was confirmed by ESI mass spectrometry, lyophilized, and kept at -80 °C.

Azobenzene Conjugation

Conjugation of the azobenzene photoswitch to the peptide was achieved through standard thiol-maleimide conjugation protocols following previously published methods.[21, 22] An excess of the photoswitch was added to encourage the coupling of a single peptide to the maleimide-modified azobenzene. The peptide-photoswitch hybrid was isolated from the reaction mixture through centrifuge filtration with Amicon Ultra-0.5 Centrifugal Filter Devices with a 3000 NMWL cut off pore size (Millipore). The remaining retentate was diluted with ~2 mL of water, lyophilized, and stored at -80°C.

Bimetallic Nanoparticle Synthesis and Photoswitching

Bimetallic NPs were prepared via coreduction of the metal ions in the presence of the peptide. For this, five different samples that varied the Pd:Au ratio were generated, including Pd:Au ratios of 1:0, 3:1, 1:1, 1:3, and 0:1. The production of the materials with a Pd:Au ratio of 3:1 is described; however, identical approaches were employed to prepare all of the structures that varied just the amount of metal ions added to the reaction mixture. To generate the materials, the peptide-photoswitch hybrid was dissolved in water to a concentration of 0.25 mM to generate a stock solution. From this, 2.0 mL of the peptide stock was diluted with 2.96 mL of water. Next, 7.5 μL of 100 mM K_2PdCl_4 and 2.5 μL of 100 mM $HAuCl_4$ was added. The reaction was allowed to stir for 15 min on the bench top, allowing for the metal ions to complex to the peptides. To reduce the metal ions and form the NPs, 30 μL of $NaBH_4$ (0.10 M, freshly prepared) was added and the sample was gently mixed three time via swirling by hand. The reaction was subsequently allowed to sit for 1 h at room temperature, unperturbed, to fully reduce.

Once prepared, photoswitching of the surface bound peptide was processed. For *trans* to *cis* switching, the peptide-capped NPs were irradiated with UV light (365 nm) for 30 min. Alternatively, *cis* to *trans* switching was achieved via irradiation with visible white light for 30 min. The photostationary state was achieved in both switching experiments, which was confirmed through UV-vis analysis.

Characterization

Characterization of the NPs was performed on the samples 24 h after reduction. UV-vis analysis was conducted using an Agilent 8453 UV-vis spectrophotometer employing 1 cm pathlength quartz cuvettes. TEM imaging was completed using either a Tecnai F30 TEM by FEI operating at 300 kV or a Talos-200FX TEM (Thermo Fisher Scientific), operated at an accelerating voltage of 200 kV. Elemental mapping was also performed by X-ray energy dispersive spectroscopy (XEDS) using ChemiSTEM™ technology, which enables fast acquisition with high sensitivity and spatial resolution. The samples were prepared by drop-casting 10 μL of the NP solution onto carbon-coated copper TEM grids, which was then allowed to dry.

XAFS spectroscopy was used to provide local chemical and structural information for Au and Pd atoms in the bimetallic NPs. The samples were sealed in a sample holder and measured at the QAS beamline (7-BM) at the National Synchrotron Light Source-II (NSLS-II) at Brookhaven National Laboratory with the spot size of the beam equal to 4 mm (w) × 2 mm (h). Au L_2-edge (used instead of the Au L_3-edge due to a monochromator glitch in the L_3-edge energy region) and Pd K-edge X-ray absorption spectra were measured in fluorescence mode using a PIPS detector. For each sample and absorption edge, at least 50 scans were collected. Au and Pd foils were measured in the same experiments in reference mode for energy calibration and alignment.

Catalytic Analysis

The catalytic properties of the three bimetallic peptide-capped NPs were evaluated through the reduction of 4-nitrophenol as a model reaction system following previously established protocols.[24] Briefly, 975 μL of water and 450 μL of NP solution were combined in a quartz cuvette, resulting in a 60 μM NP suspension based upon total metal content. The particle solution was allowed to incubate for ~10-15 min until the desired temperature was reached, at which point 25 μL of freshly prepared $NaBH_4$ (3.6 M) was added, resulting in a 60 mM concentration. After a 10 min incubation period, 50 μL of 4-nitrophenol (3.6 mM) was mixed into the solution, resulting in a reaction concentration of 120 μM substrate with a significant excess of $NaBH_4$. UV-vis analysis of the reaction progression was completed where the substrate absorbance intensity at 400 nm was monitored until reaction completion. Each reaction was performed in triplicate where the average rate constants are reported ± one standard deviation.

Results and discussion

To couple the azobenzene-based photoswitch into the AuBP1 peptide, thiol maleimide coupling was processed.[21, 22] Briefly, the azobenzene molecule was modified with two terminal maleimide groups to generate the maleimide-azobenzene-maleimide (MAM) molecule, as previously described.[21] To incorporate this into to the peptide, a cysteine residue was appended to the C-terminus of the AuBP1 sequence (termed AuBP1C). Subsequent coupling between the thiol and MAM was processed using a stoichiometric excess of MAM to ensure a single coupling event. Once prepared, the AuBP1C-MAM molecule was used to generate the inorganic NPs (Scheme 1). For this, coreduction of Au^{3+} and Pd^{2+} at selected ratios was processed in the presence of the peptide, leading to a stable colloidal suspension of materials. The Pd:Au ratio varied from 100% Pd to 100% Au where each individual system is distinguished by the Pd:Au ratio used to prepare the sample. For this, five samples were prepared at ratios of 1:0, 3:1, 1:1, 1:3, and 0:1 Pd:Au.

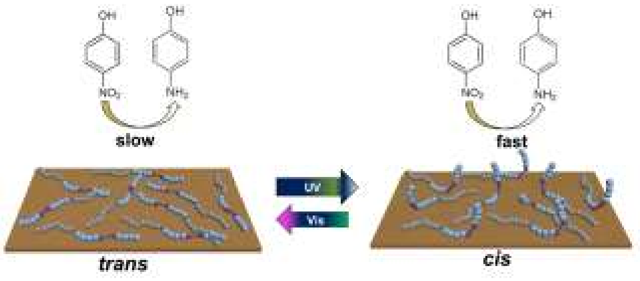

Scheme 1. Representation of peptide overlayer conformational changes in response to peptide photoswitching, leading to changes in catalytic performance.

NP synthesis was initially examined at each major step with UV-vis spectroscopy (Figure 1). As shown in Figure 1a (left panel) for particles prepared at a 1:0 Pd:Au ratio, the peptide-photoswitch conjugate in water displayed a strong absorbance centered at 336 nm and a weaker band at 450 nm (black spectrum). These two absorbances are the signature features of azobenzene, arising from the π-π* and n-π* transitions, respectively.[26] Upon Pd^{2+} metal ion addition and complexation to the peptide (red spectrum), no major changes in absorbance were noted as compared to the peptide solution; however, a shoulder band at 275 nm was observed, likely arising from a ligand to metal charge transfer band between Pd and Cl.[27] After reduction and NP formation (blue spectrum), an increase in absorbance toward lower wavelengths was observed, consistent with particle formation.[28] Additionally, the π-π* transition of the azobenzene moiety also was observed in the sample. Note that the n-π* azobenzene transition was not

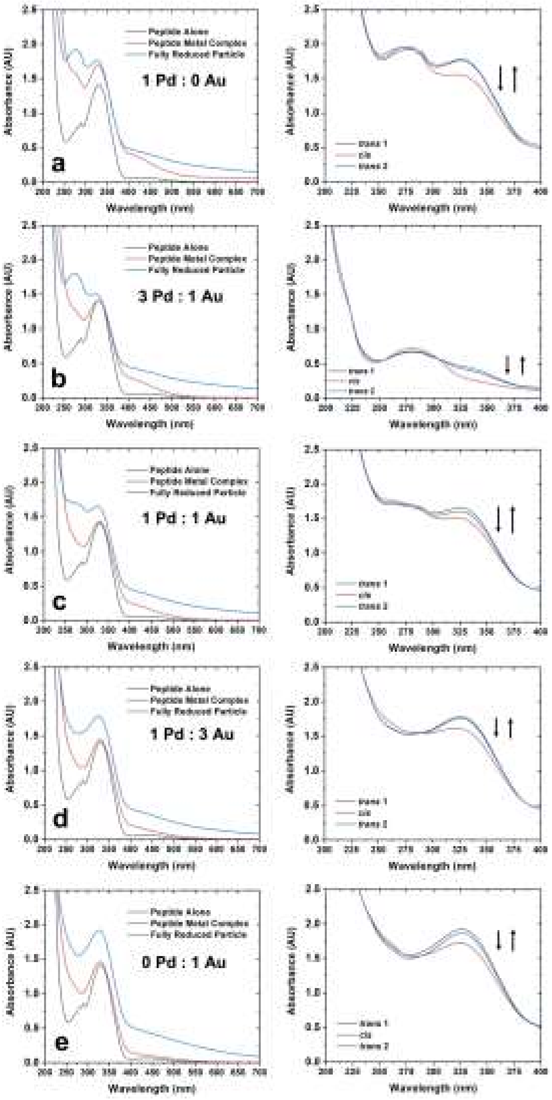

Figure 1. UV-vis analysis of peptide-based NP synthesis (left) and photoswitching analysis of the azobenzene moiety of the peptide bound to the NP (right) for the materials prepared at a Pd:Au ratio of (a) 1:0, (b) 3:1, (c) 1:1, (d) 1:3, and (e) 0:1.

visible in the NP sample due to the inherent absorbance of the materials. Interestingly, the absorbance at 275 nm remained after reduction, suggesting that a portion of the Pd^{2+} ions remained unreduced and complexed with Cl^{-}. Similar effects of incomplete Pd ion reduction were previously noted for other peptide-capped Pd NPs.[29]

For the preparation of the bimetallic materials at Pd:Au ratios of 3:1, 1:1, and 1:3 (Figure 1 b-d), similar results as compared to the monometallic Pd NPs were observed. Comparatively, as the amount of Au in the sample increased, the intensity of the Pd-Cl coordination peak at 275 nm after reduction decreased, where it was not observed in the materials prepared at a 1:3 Pd:Au ratio. Such effects are anticipated as fewer Pd ions should be present in the sample. Finally, for the monometallic Au NPs prepared at a Pd:Au ratio 0:1 (Figure 1e), no localized surface plasmon resonance (LSPR) band was noted for the reduced materials (blue spectrum), indicating that the particles are likely to be quite small in size.

Following NP production, the photoswitch functionality was examined via UV-vis spectroscopy. Under irradiation with either UV or white light, the azobenzene component of the biomolecule can isomerize from *trans*-to-*cis* or *cis*-to-*trans,* respectively.[20, 21, 26] To confirm the photoswitching process, the intensity of the 336 nm peak can be monitored. To this end, the 336 nm peak intensity will decrease during *trans* to *cis* switching; however, the intensity will increase during *cis* to *trans* switching. For the peptide-capped NPs prepared at a Pd:Au ratio of 1:0 (Figure 1a, right panel), changes in the absorption intensity after photoswitching were examined. As anticipated, the intensity of the π-π^* peak decreased under UV light; however, after illumination of the sample with visible light, the 320 nm peak return to its original intensity. Such photo-based switching effects were observed across all of the other NPs prepared at the different Pd:Au ratios (Figure 1b-e, right panel), confirming that the photoswitch remained active once bound to the NP surface, regardless of the material composition.

TEM analysis of the prepared NPs was completed to observe the overall structure of the materials, as presented in Figure 2. For the Pd NPs prepared at a Pd:Au ratio of 1:0 (Figure 2a), spherical structures were observed with an average diameter of 4.5 ± 1.8 nm. For the PdAu bimetallic materials, spherical NPs were again observed with diameters of 3.1 ± 1.1, 2.8 ± 1.2, and 3.1 ± 1.3 nm for the structures prepared at Pd:Au ratios of 3:1, 1:1, and 1:3, respectively. Finally, for the monometallic Au NPs generated at a Pd:Au ratio of 0:1, particles with an average diameter of 2.1 ± 1.0 nm were noted. For all samples, analysis of >100 particles was used to identify the average particle sizes, as shown in the histograms of Figure 2. High-resolution TEM (HR-TEM) of the bimetallic PdAu NPs is also included as insets of Figure 2b-d. For each system, crystallinity of the NPs is evident from the lattice fringes revealed in the images in the insets.

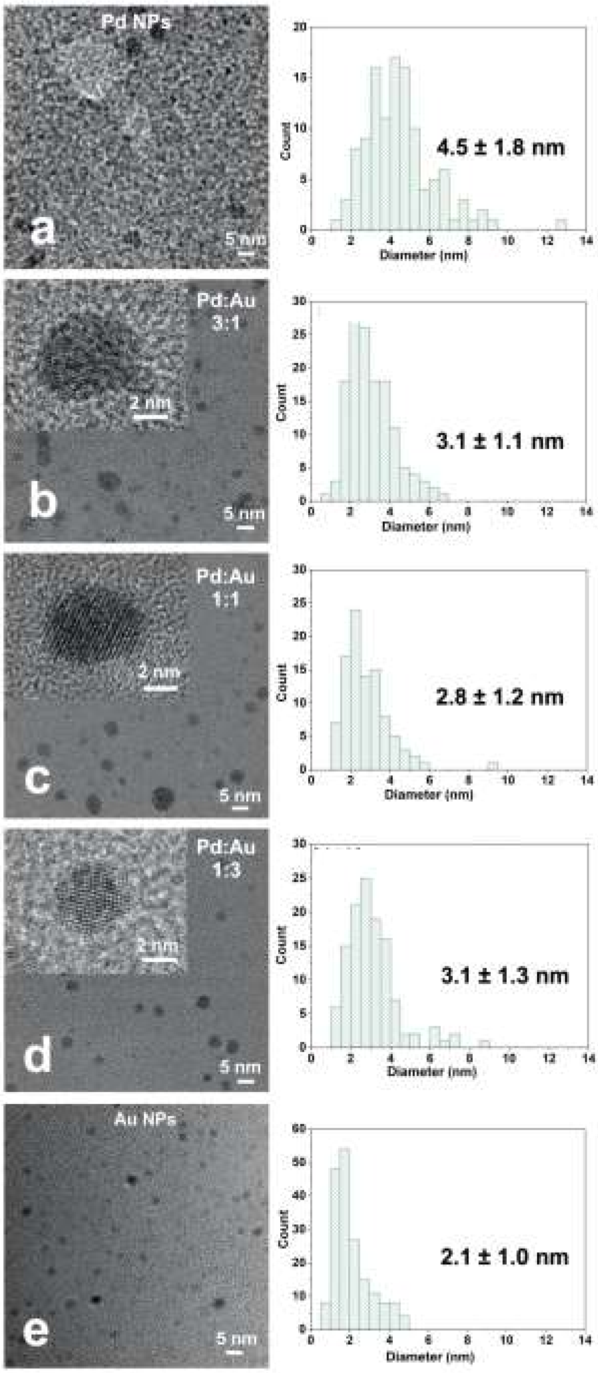

Figure 2. TEM analysis of the peptide-capped NPs prepared at a Pd:Au ratio of (a) 1:0, (b) 3:1, (c) 1:1, (d) 1:3, and (e) 0:1. The left panel presents the TEM image, while the right panel presents the particle size histogram. Insets display a high resolution TEM image of the indicated sample.

To gain an understanding on the Pd-Au composition in the final bimetallic NPs, XEDS mapping of the structures prepared at a Pd:Au ratio of 3:1 was processed. Figure 3 presents the high-angle annular dark field (HAADF) image of the particles, where the Au and Pd maps of the particles are displayed in red and green, respectively. Overlaying of the maps demonstrates localization of both Pd and Au in the NPs, confirming that both elements were present within the material. While EDS mapping did confirm the co-localization of the Pd and Au in the NPs, it could not provide the atomic organization of the different metal atoms within the individual particles nor did it allow for quantification the composition of Pd and Au within the particles.

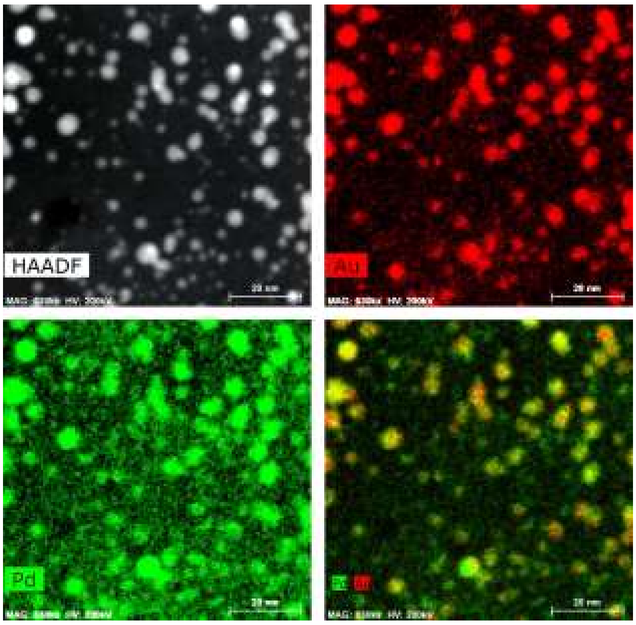

Figure 3. XEDS mapping analysis of the peptide-capped PdAu NPs prepared at a Pd:Au ratio of 3:1. The HAADF image of the NPs is presented in the upper left, while the Au and Pd maps are presented in red and green, respectively. An overlay of the Pd and Au regions is shown in the bottom right, confirm colocalization of the two metals in the NPs.

To elucidate the atomic structure of the PdAu materials, XAFS spectroscopy was used to provide local chemical and structural information for the Au and Pd atoms in the bimetallic materials. For this, the QAS beamline (7-BM) at the National Synchrotron Light Source-II (NSLS-II) at Brookhaven National Laboratory was used. For Au studies, the L_2 edge was examined because of the monochromator glitch at the L_3 edge. X-ray absorption near-edge structure (XANES) spectra at the Au L_2-edge and Pd K-edge are shown in Figure 4a and b, respectively. In all samples, Au appears to be in the zerovalent state, based on the similarity of the features in the peak maximum (white line) region. After background subtraction and edge-step normalization, the EXAFS data were converted to *k*-space. The k^2-weighted spectra (Supporting Information, Figure S1) were Fourier transformed to r-space (Figure 4c). The split peak between 1.5 and 3.5 Å in the EXAFS spectrum of the Au foil standard represents the nearest neighboring Au-Au bond. With the increase of Au in the materials, the intensity of left peak increases and the right peak decreases (Figure 4c), consistent with the change in the Pd:Au ratio towards Au-rich material.

XANES data at the Pd K-edge (24.35 keV) show that Pd is largely nonmetallic in the NPs, in contrast to the bulk Pd (Figure 4b). In the EXAFS spectra (Figure 4d), the split peak between 1.5 and 3.0 Å in the EXAFS spectrum of Pd foil standard corresponds to the Pd-Pd first nearest neighboring bond. For the bimetallic materials, a drastically different local environment (on average) is evident through the broad peak between 1.0 and 2.2 Å, likely to be caused by predominant coordination of a low Z ligand, in agreement with the trend shown in Pd K-edge XANES data (Figure 4b). This coordination by a low Z ligand is consistent with the observation of a peak at 275 nm in the UV-vis spectra of the bimetallic materials, consistent with Pd-Cl bonds.[27]

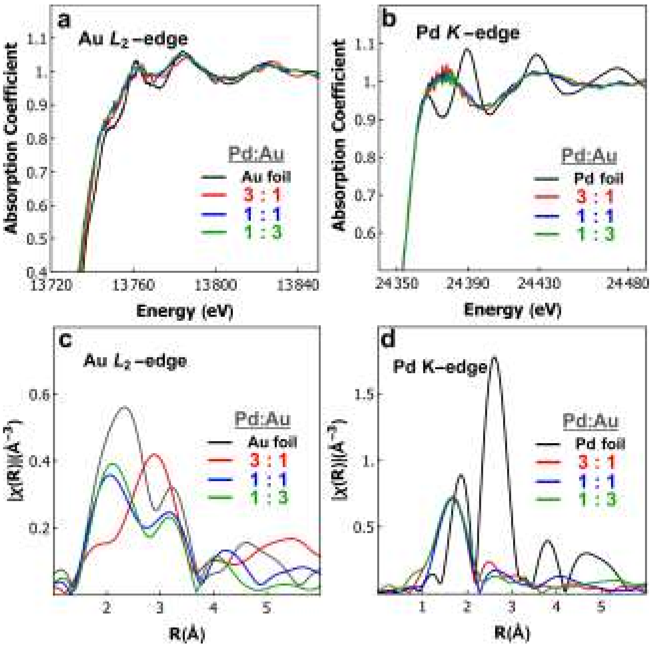

Figure 4. XANES spectra at the (a) Au L_2-edge and (b) Pd K-edge. Fourier transform magnitudes of k^2-weighted EXAFS spectra at the (c) Au L_2-edge (d) Pd K-edge.

To model the local environment around Au and Pd in the bimetallic samples, we used the Artemis program of Demeter package (Supporting information Figure S2).[30] For the Au L_2-edge data analysis, theoretical metal-metal contributions only were used, as suggested by the data (Figure 4c); however, for the Pd K-edge data analysis, only metal-nonmetal contribution was considered in the model. In addition to varying the coordination numbers, corrections to the bond distances and their mean square deviations, σ^2, varied correction to the photoelectron energy origin was also used in the fit. In order to minimize the uncertainties and increase confidence in the results, a multiple data set fitting model was used in which the Au-Pd and Au-Au σ^2 variables were constrained to be unique for each type of a pair but the same for all bimetallic compositions. Furthermore, the best fit value (1.0) for the amplitude reduction factor from analysis of Au foil was used and fixed to that value in the fit of the bimetallic catalysts. The fitting *k*-ranges and *r*-ranges are presented in the Supporting Information (Table S1). For Pd edge data, the best fit value (0.74) was used for the amplitude reduction factor from analysis of Pd foil and fixed to that value in the fit of the bimetallic catalysts. More fitting details are included in the Supporting Information.

The results are summarized in Table 1. As expected from the trends in the raw data (Figure 4c), as the amount of Au in the sample decreases, the Au-Au coordination number (CN) decreases and Au-Pd CN increases. However, because the Pd edge data demonstrated that not all Pd atoms are in NPs, in order to understand the distribution of Pd atoms in the particles, the CNs of Au-Pd bonds within the NPs should be used, not the ensemble-average Au-Pd CN obtained by our fitting. To probe the distribution of our bimetallic materials, we obtained the information of Pd-nonmetal CNs first. For that, it was assumed that nonmetallic neighbors to Pd originate from

Table 1. EXAFS analysis results for the bimetallic PdAu NPs at the Au L_2- edge and Pd K-edge. Other results include the actual ratio (x_{NP}) of Pd:Au in the PdAu NPs, the ratio of the coordination numbers of the Au-Au to Au-Pd pairs, and the short range order parameter (α).

Sample (Pd : Au)	CN (Au-Au)	CN (Au-Pd)	CN (Pd-Cl)	χ_{NP} Ratio (Pd : Au)	CN(Au-Au)/ CN(Au-Pd)	α
3:1	2.0 ± 1.6	3.2 ± 1.7	3.5 ± 0.6	0.375	0.63 ± 0.6	-1.25
1:1	4.1 ± 2.0	1.2 ± 0.7	3.5 ± 0.5	0.125	3.4 ± 2.6	-1.04
1:3	4.8 ± 2.2	0.9 ± 0.5	3.8 ± 0.5	0.017	5.3 ± 3.8	-8.45

the unreduced precursor, K_2PdCl_4, and used the fraction of Pd atoms associated with Cl^- to understand the distribution of Pd in the NPs.[31] We first translated the measured CN_{Pd-Cl} in terms of the ratio of Pd atoms in the PdAu NPs:

$$CN_{Pd-Cl} = \frac{4N_{Pd-sol}}{N_{Pd-sol}+N_{Pd-np}} \qquad (1)$$

$$y = \frac{N_{Pd-np}}{N_{Pd-sol}+N_{Pd-np}} = 1 - \frac{CN_{Pd-Cl}}{4} \qquad (2)$$

where $N_{Pd\text{-}sol}$ is the total number of Pd in K_2PdCl_4, $N_{Pd\text{-}np}$ is the total number of Pd in PdAu NPs, and *y* is the fraction of Pd atoms in the PdAu NPs with respect to the total number of Pd atoms in the sample, N_{Pd}. The ratio x_{NP} of Pd:Au in PdAu NPs was calculated according to the Eq. 3:

$$x_{NP} = \frac{N_{Pd-np}}{N_{Au}} = \frac{y{*}N_{Pd}}{N_{Au}} \qquad (3)$$

where N_{Au} is the total number of Au in the sample, all of them – in the PdAu NPs. Finally, we combined the result listed in Table 1 to decide whether the Pd and Au in the NP was alloyed or segregated. Using a short-range order parameter definition:[32-34]

$$\alpha = 1 - \frac{CN_{Au-Pd}/(CN_{Au-Pd}+CN_{Au-Au})}{x_{Pd}} \qquad (4)$$

where X_{Pd} is the actual concentration of Pd in PdAu NPs and α is the Cowley order parameter, the degree of short-range order or tendency to clustering can be investigated; if $\alpha > 0$, then the alloyed components tend to segregate and vice versa. From the result in Table 1, we concluded that bimetallic NPs prepared at Pd:Au ratios of 3:1 (α = -1.25), 1:1 (α = -1.04), and 1:3 (α = -8.45) form a fully alloyed structure. Such results are fully consistent with the EDS-mapping data that confirmed the presence of both Pd and Au in the sample; however, it provides atomically-resolved information confirming the mixing of the two metals in the NP samples.

With confirmation of the structures of the different peptide-capped NPs, the catalytic reactivity of the bimetallic NPs was determined in both the *trans* and *cis* photoswitch conformations. This reactivity was directly compared to the reactivity for the monometallic Pd and Au NPs (1:0 and 0:1 ratios, respectively), which was previously reported.[22, 24] For this, the model reduction of 4-nitrophenol to 4-aminophenol was studied (Figure 5a), which takes place directly on the particle metal surface following a Langmuir-Hinshelwood mechanism.[35] As such, this provides a direct method for interrogating how the effects of the peptide interface conformation and the bimetallic composition impact catalysis.

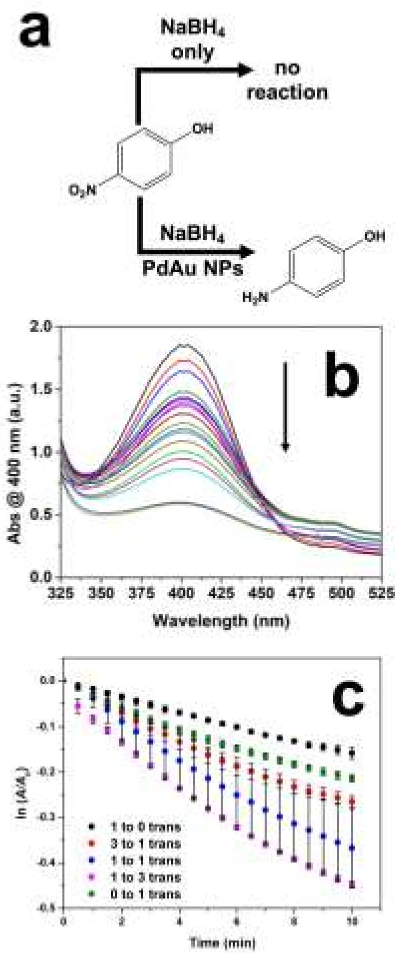

Figure 5. Catalytic analysis of the peptide-capped PdAu NPs. Part (a) presents the model 4-nitrophenol reduction reaction. Part (b) displays the change in the UV-vis spectrum of the reaction showing the decrease in absorbance over time associated with substrate consumption. Part (c) shows the change in absorbance of the reactions catalyzed by the PdAu NPs as a function of time to determine individual k_{obs} values.

For the reaction using the *cis*-based materials, the bimetallic NPs were irradiated to reach the *cis* photostationary state. The reaction was subsequently run as described. The half-lives of the monometallic Pd and Au NPs capped with AuBP1C-MAM in the *cis* conformation are both >67 h,[22, 24] thus the vast majority of the peptides will remain in the *cis* conformation over the 10 min 4-nitrophenol reduction reaction studied herein.

For this reaction, the bimetallic NPs in the appropriate conformation are incubated with $NaBH_4$ for 10 min, after which the 4-nitrophenol substrate was added to the system, initiating the reaction. It is important to note that the $NaBH_4$ is in significant excess, thus the reaction is *pseudo* first order with respect to the substrate, consistent with literature precedent.[24, 35, 36] The reaction is readily monitored using UV-vis via the decrease in substrate absorbance at 400 nm (Figure 5b), from which plots of $\ln(A/A_0)$ vs time (A = absorbance at time t, A_0 = initial absorbance) can be used to extract rate constants (k_{obs}). Figure 5c presents a comparison of the $\ln(A/A_0)$ vs time plot for all of the different NPs studied at a temperature of 20 °C with the peptide in the *trans* conformation. From this qualitative comparison, it is evident that significant differences in the reactivity are observed as a function of material composition.

Using the plots of $\ln(A/A_0)$ *vs* time, abstraction of the rate constants over a reaction temperature range of 15 – 35 °C was processed for the bimetallic NPs in the *trans* and *cis* conformation. These values were subsequently compared to previously identified rate constants for the monometallic Pd and Au systems.[22, 24] Comparing the k_{obs} values at a temperature of 20 °C with the peptide in the *trans* conformation demonstrates a unique reactivity trend (Figure 6a). In this regard, for the Pd monometallic materials prepared at a Pd:Au ratio of 1:0, a rate constant of (14.7 ± 1.5) x 10^{-3} s^{-1} was reported,[22] which increased to (27.1 ± 1.5) x 10^{-3} s^{-1} for the bimetallic NPs prepared at a Pd:Au ratio of 3:1. As the Pd:Au ratio increased to 1:1 and 1:3, the k_{obs} values further increased to (32.1 ± 1.0) x 10^{-3} and (38.7 ± 0.01) x 10^{-3} s^{-1}, respectively. Subsequently, for the monometallic Au NPs prepared at a Pd:Au ratio of 0:1, the rate constant was substantially lower, with a value of (9.0 ± 1.3) x 10^{-3} s^{-1} as demonstrated previously.[24] This trend suggests that the materials prepared at a Pd:Au ratio of 1:3 displayed maximal reactivity with the peptide in the *trans* conformation. Such results were generally consistent at higher temperatures, but with increased k_{obs} values, as anticipated. It is interesting to note, though, that for the NPs prepared at a Pd:Au ratio of 1:1, a linear increase in reactivity was not observed with increasing temperatures, especially at the highest temperature studied (35 °C, Supporting Information, Table S2). This suggests that the NPs may not be stable at elevated temperatures.

When the peptide was switched to the *cis* conformation, a similar trend in k_{obs} values was noted based upon the material composition. As shown in Figure 6b at a temperature of 20 °C, the monometallic Pd materials (Pd:Au ratio of 1:0) were shown to have a rate constant of (10.5 ± 1.5) x 10^{-3} s^{-1} from prior results.[22] For the bimetallic materials, k_{obs} values of (33.2 ± 1.4) x 10^{-3}, (32.0 ± 0.4) x 10^{-3}, and (53.8 ± 2.0) x 10^{-3} s^{-1} were noted for the Pd:Au samples of 3:1, 1:1, and 1:3 ratios, respectively. As anticipated, the reactivity greatly diminished for the monometallic Au sample (Pd:Au ratio of 0:1), with a reported k_{obs} of (4.2 ± 0.7) x 10^{-3} s^{-1}.[24] This trend of maximum reactivity for the Pd:Au ratio 1:3 sample remains for the particles in the *cis* conformation, where this reactivity was slightly higher for the *cis* bimetallic NPs as compared to their *trans* counterparts (*vide infra*). Similar to the *trans*-based materials, increased reactivity was noted at higher temperatures; however, the Pd:Au 1:1 NPs deviated from the reactivity trend. These samples demonstrated diminished reactivity as compared to the Pd:Au 3:1 sample at higher temperatures; however, this is likely attributed to NP instability under these elevated temperature conditions.

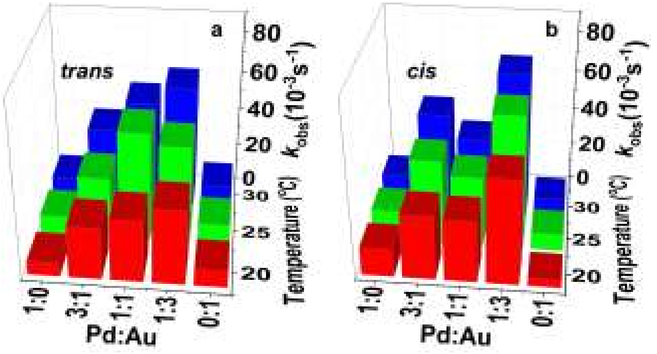

Figure 6. Comparison of rate constants for the bimetallic peptide-capped NPs prepared at the indicated ratios as a function of reaction temperature for the peptides in the (a) *trans* and (b) *cis* conformations.

Taken together, as the amount of Au in the bimetallic material increased, higher reaction rates were generally observed. When the particles were prepared at the Pd:Au 3:1 ratio (Figure 6 and Supporting Information, Table S2), the NPs with the *cis* peptide conformation demonstrated a linear increase in k_{obs} values ranging from (24.4 ± 3.3) × 10^{-3} s^{-1} to (66.9 ± 1.6) × 10^{-3} s^{-1} over a 15°C to 35°C temperature range. A less substantial increase was noted for the same NPs with the peptide overlayer in the *trans* conformation, where at 15 °C the average rate constant was (21.4 ± 7.1) × 10^{-3} s^{-1}, which increased to (48.4 ± 9.2) × 10^{-3} s^{-1} at 35°C (Supporting Information, Table S2). From an Arrhenius plot of these analyses, an activation energy of 29.2 ± 5.1 kJ/mol was calculated for the *trans* isomer, which was smaller than the E_a for the *cis* state (36.3 ± 2.8 kJ/mol). This suggests that another factor beyond the activation energy drives the system as faster reactivity was noted from the system with a greater E_a value. As such, the pre-exponential factors (A) for both systems were determined where values of 4.3 × 10^3 and 9.7 × 10^4 s^{-1} were identified for the *trans*- and *cis*-based bimetallic NPs prepared at a Pd:Au ratio of 3:1, respectively. From these E_a and A values, this suggests that the system is dominated by the differences in the pre-exponential factors between the particles in the *cis* and *trans* conformation (Table 2).

The highest reaction rates for 4-nitrophenol reduction were observed for the bimetallic particles prepared at a Pd:Au ratio of 1:3 (Figure 6). For this system, the rate constants ranged from (28.6 ± 1.5) × 10^{-3} to (72.5 ± 0.3) × 10^{-3} s^{-1} from 15 – 35 °C for the NPs with the peptide in the *trans* conformation and from (43.3 ± 2.5) × 10^{-3} to (85.2 ± 2.0) × 10^{-3} s^{-1} for the same NPs with the *cis* conformation of the bio-overlayer. For this system, the E_a value was lower for the *cis* state (24.9 ± 2.1 kJ/mol) compared

Table 2. Comparison of E_a and A values for the indicated PdAu bimetallic peptide-capped NP catalysts

	trans[a,b]		*cis*[a,b]	
Pd:Au	E_a (kJ/mol)	A (s^{-1})	E_a (kJ/mol)	A (s^{-1})
1:0	30.9 ± 5.1	2.2×10^3	16.6 ± 2.9	1.3×10^1
3:1	29.2 ± 5.1	4.3×10^3	36.3 ± 2.8	9.7×10^4
1:1	---	---	16.8 ± 2.9	3.3×10^1
1:3	34.7 ± 1.8	5.8×10^4	24.9 ± 2.1	1.5×10^3
0:1	23.0 ± 3.5	---	35.3 ± 4.0	---

a. Data for the 1:0 sample previously reported from ref 22.
b. Data for the 0:1 sample previously reported from ref 24.

to the *trans* state (34.7 ± 1.8 kJ/mol); however, the *A* value was greater for the *trans* conformation (5.8×10^4 s^{-1}) over the *cis* (1.5×10^3 s^{-1}). In this specific situation, the system is dominated by the activation energy differences, resulting in faster reactivity for the NPs with the peptide in the *cis* configuration, which is the opposite factor (E_a vs *A*) as compared to the NPs prepared at a Pd:Au ratio of 3:1. To this end, while both systems displayed greater reactivity for the NPs with the *cis*-based peptide, the *A* value was the dominating force for the Pd:Au 3:1 NPs, while the activation energy was responsible for controlling the reactivity for the Pd:Au 1:3 NPs. This suggests that the reactivity differences between the *cis* vs. *trans* conformation can be controlled by different factors based upon the NP composition and potentially how it affects the peptide conformation in the two isomerization states.

Finally for the NPs prepared at Pd:Au ratio of 1:1, clear differences in reaction rate constants were observed, suggestive of particle instability at elevated temperatures (Supporting Information, Table S2). While the NPs with the peptide in the *cis* conformation gave rise to a linear increase in k_{obs} values over the selected reaction temperature range ((29.3 ± 3.1) × 10^{-3} s^{-1} to (46.6 ± 3.5) × 10^{-3} s^{-1}) a non-linear trend was observed for the same NPs in the *trans* conformation. For the *trans*-based materials, the k_{obs} values did increase from (20.5 ± 2.1) × 10^{-3} s^{-1} at 15°C to 56.2 ± 2.2 s^{-1} at 25 °C; however, as the temperature further increased to 35°C, the reaction rate decrease to 41.3 ± 5.5 s^{-1}. This lack of linearity at elevated temperatures indicates that the materials are unstable at higher temperatures, which prevents calculation of the E_a and *A* values. For the NPs with the peptides in the *cis* conformation, an activation energy of 16.8 ± 2.9 kJ/mol and a preexponential factor of 3.3×10^1 s^{-1} were determined; however, due to the lack of stability of the *trans*-based materials, this suggests that the 1:1 NPs may be not directly comparable to the other bimetallic materials.

When comparing the E_a and *A* values for the bimetallic NPs reported herein with their monometallic counterparts previously reported, such values are generally quite similar. For instance, for the monometallic Au materials (Pd:Au ratio of 0:1), substantially diminished reactivity was observed compared to the bimetallic structures (Figure 6). In this regard, for the materials with the peptide in the *trans* and *cis* configurations, E_a values of 23.0 ± 3.5 and 35.3 ± 4.0 kJ/mol, respectively, have been reported.[24] In general, this system is dominated by the activation energy where greater reactivity for the *trans* material over the *cis* has been noted. For the monometallic Pd structures, an E_a value of 30.9 ± 5.1 kJ/mol for the *trans* has been reported, which is higher than the value for the *cis* structures (16.6 ± 2.9 kJ/mol).[22] This system also demonstrated *A* values of 2.2×10^3 and 1.3×10^1 s^{-1} for the *trans* and *cis*-based materials, respectively.[22] Since these materials demonstrated greater reactivity for the *cis* over *trans* configuration, this indicates that the activation energy controls the overall reactivity of the materials.

With an understanding of the reactivity trends, the recyclability of the materials for catalytic reactivity was probed using the bimetallic materials prepared at a Pd:Au ratio of 1:3. This system was chosen as it was noted to be the most reactive. For this analysis, the reaction was processed using the materials with the peptide in the *trans* conformation over seven reaction cycles, where the reactivity remained roughly equivalent after the seventh cycle (Supporting Information, Figure S3). This suggests that the bimetallic NPs retain the reactivity over multiple catalytic reactions, which is highly important for long term use.

While it is clear that greatest reactivity was observed for the NPs with the peptides in the *cis* configuration with a Pd:Au ratio of 1:3, it is important to compare these observations with comparable materials. Several reports have focused on the use of PdAu bimetallic NPs for the reduction of 4-nitrophenol.[37-42] In all cases, the bimetallic materials outperformed their monometallic counterparts. For instance, Ballauff and coworkers employed PdAu bimetallic NPs that were embedded within spherical polyelectrolyte brushes.[38] Using this system, they demonstrated maximum reduction of 4-nitrophenol using the PdAu bimetallic NPs with a Pd:Au ratio of 1:3. In separate work, Wang *et al.* catalyzed the reaction using PdAu particles that were supported on activated carbon.[39] In this case, the materials with a Pd:Au ratio of 1:9 presented the highest turnover frequency for the reduction of 4-nitrophenol. In both cases, such results are quite consistent with the present study that demonstrated maximum k_{obs} values using the peptide-capped particles with a Pd:Au ratio of 1:3.

It is interesting to note that in separate work using PdAu bimetallic NPs, materials with different Pd:Au ratios displayed maximized 4-nitrophenol reduction efficiency. For instance, Chen *et al.* demonstrated optimized reactivity using PdAu NPs on graphene sheets with a Pd:Au ratio of 1:1.[37] Similarly, Fang *et al.* saw PdAu NPs prepared at a 1:1 ratio of the metals displayed maximum reactivity compared to other ratios.[40] In this case, the materials were deposited onto graphitic C_3N_4 nanosheets for colloidal stability. This suggests that the underlaying material that the bimetallic NPs interacts with can attenuate the catalytic reactivity, especially when using highly conductive systems such as graphene and C_3N_4. Such effects are also highlighted herein using the peptides. In this case, differences in reactivity for the same NP composition were noted based upon the conformation of the bioligand overlayer structure (*cis* vs. *trans*); however, the trend in bimetallic composition effects were the same between both systems with maximum reactivity at a Pd:Au ratio of 1:3. This suggests that the differences in reactivity based upon the *cis*/*trans* conformation is likely an effect of the peptide conformational structure.

Conclusions

In conclusion, the fabrication of PdAu bimetallic NPs with a photoswitch/peptide hybrid biomolecule was demonstrated, where the reactivity of the system is dependent upon both the material composition and peptide conformation. Using this approach, bimetallic structures were prepared wherein the two metal components were alloyed together. Catalytic analysis of the structure using the reduction of 4-nitrophenol as a model system indicated that maximum reactivity was achieved for the NPs prepared at a Pd:Au ratio of 1:3, consistent with prior studies. This reactivity could be modulated via photoswitch isomerization where enhanced reactivity was observed for the NPs with the peptide in the *cis* conformation. This was controlled through changes in either the activation energy or pre-exponential factor of the system. Taken together, these results provide pathways towards the production of intriguing materials of various compositions where their properties are tuneable via light-activation. Such capabilities could prove to be important for a variety of catalytic reactions, as well as other systems where having the NP surface in two conformations could prove to be advantageous (e.g. biosensing, nanomedicine, etc.).

Conflicts of interest

There are no conflicts to declare.

Acknowledgements

This material is based upon work supported by the National Science Foundation under Grant Nos CHE-1903649 to MK and CHE-1903576 to AIF. The XAS data were acquired at beamline 7-BM (QAS) of the National Synchrotron Light Source II (NSLS-II), a U.S. DOE Office of Science User Facility operated for the DOE Office of Science by Brookhaven National Laboratory (BNL) under Contract No. DE-SC0012704. The QAS beamline operations were supported in part by the Synchrotron Catalysis Consortium (U.S. DOE, Office of Basic Energy Sciences, grant number DE-SC0012335).

Notes and references

1. C. Xie, Z. Niu, D. Kim, M. Li and P. Yang, *Chem. Rev.*, 2020, **120**, 1184-1249.
2. M. Sankar, Q. He, R. V. Engel, M. A. Sainna, A. J. Logsdail, A. Roldan, D. J. Willock, N. Agarwal, C. J. Kiely and G. J. Hutchings, *Chem. Rev.*, 2020, **120**, 3890-3938.
3. R. Bhandari, D. B. Pacardo, N. M. Bedford, R. R. Naik and M. R. Knecht, *J. Phys. Chem. C*, 2013, **117**, 18053-18062.
4. R. Bhandari and M. R. Knecht, *Catal. Sci. Technol.*, 2012, **2**, 1360-1366.
5. O. M. Wilson, M. R. Knecht, J. C. Garcia-Martinez and R. M. Crooks, *J. Am. Chem. Soc.*, 2006, **128**, 4510-4511.
6. G. Totarella, R. Beerthuis, N. Masoud, C. Louis, L. Delannoy and P. E. de Jongh, *J. Phys. Chem. C*, 2021, **125**, 366-375.
7. H. S. Choi, J. Lee, D. Kim, A. Kumar, B. Jeong, K.-J. Kim, H. Lee and J. Y. Park, *Catal. Sci. Technol.*, 2021, ASAP.
8. A. M. Pennington, C. L. Pitman, P. A. DeSario, T. H. Brintlinger, S. Jeon, R. B. Balow, J. J. Pietron, R. M. Stroud and D. R. Rolison, *ACS Catal.*, 2020, **10**, 14834-14846.
9. B. D. Briggs, N. M. Bedford, S. Seifert, H. Koerner, R. R. Naik, A. I. Frenkel and M. R. Knecht, *Chem. Sci.*, 2015, ASAP.
10. N. Norouzi, M. K. Das, A. J. Richard, A. A. Ibrahim, H. M. El-Kaderi and M. S. El-Shall, *Nanoscale*, 2020, **12**, 19191-19202.
11. N. A. Merrill, E. M. McKee, K. C. Merino, L. F. Drummy, S. Lee, B. Reinhart, Y. Ren, A. I. Frenkel, R. R. Naik, N. M. Bedford and M. R. Knecht, *ACS Nano*, 2015, in revision.
12. K. D. Gilroy, A. Ruditskiy, H.-S. Peng, D. Qin and Y. Xia, *Chem. Rev.* , 2016, **116**, 10414-10472.
13. W. Yu, M. D. Porosoff and J. G. Chen, *Chem. Rev.*, 2012, **112**, 5780-5817.
14. C. Cerezo-Navarrete, Y. Mathieu, M. Puche, C. Morales, P. Concepción, L. M. Martínez-Prieto and A. Corma, *Catal. Sci. Technol.*, 2021, ASAP.
15. R. W. J. Scott, O. M. Wilson, S.-K. Oh, E. A. Kenik and R. M. Crooks, *J. Am. Chem. Soc.*, 2004, **126**, 15583-15591.
16. Y. Holade, S. Hebié, K. Maximova, M. Sentis, P. Delaporte, K. B. Kokoh, T. W. Napporn and A. V. Kabashin, *Catal. Sci. Technol.*, 2020, **10**, 7955-7964.
17. S. Bhama, T. R. Sibakoti, J. B. Jasinski and F. P. Zamborini, *ChemCatChem*, 2020, **12**, 2253-2261.
18. A. Hueur-Jungemann, N. Feliu, I. Bakaimi, M. Hamaly, A. Aklkilany, I. Chakraborty, A. Masood, M. F. Casula, A. Kostopoulou, E. Oh, K. Susumu, M. H. Stewart, I. L. Medintz, E. Stratakis, W. J. Parak and A. G. Kanaras, *Chem. Rev.*, 2019, **119**, 4819-4880.
19. T. R. Walsh and M. R. Knecht, *Chem. Rev.*, 2017, **117**, 12641-12704.
20. J. P. Palafox-Hernandez, C.-K. Lim, Z. Tang, K. L. M. Drew, Z. E. Hughes, Y. Li, M. T. Swihart, P. N. Prasad, M. R. Knecht and T. R. Walsh, *ACS Appl. Mater. Interfaces*, 2016, **8**, 1050-1060.
21. Z. Tang, C.-K. Lim, J. P. Palafox-Hernandez, K. L. M. Drew, Y. Li, M. T. Swihart, P. N. Prasad, T. R. Walsh and M. R. Knecht, *Nanoscale*, 2015, **7**, 13638-13645.
22. R. L. Lawrence, V. J. Cendan, B. Scola, Y. Liu, C.-K. Lim, P. N. Prasad, M. T. Swihart and M. R. Knecht, *J. Phys. Chem. C*, 2018, **122**, 28055-28064.
23. R. L. Lawrence, Z. E. Hughes, V. J. Cendan, Y. Liu, C.-K. Lim, P. N. Prasad, M. T. Swihart, T. R. Walsh and M. R. Knecht, *ACS Appl. Mater. Interfaces*, 2018, **10**, 33640-33651.
24. R. L. Lawrence, B. Scola, Y. Li, C.-K. Lim, Y. Liu, P. N. Prasad, M. T. Swihart and M. R. Knecht, *ACS Nano*, 2016, **10**, 9470-9477.
25. M. Hnilova, E. E. Oren, U. O. S. Seker, B. R. Wilson, S. Collino, J. S. Evans, C. Tamerler and M. Sarikaya, *Langmuir*, 2008, **24**, 12440-12445.
26. H. M. D. Bandara and S. C. Burdette, *Chem. Soc. Rev.*, 2012, **41**, 1809-1825.
27. J. J. Cruywagen and R. J. Kriek, *J. Coord. Chem.*, 2007, **60**, 439-447.
28. J. A. Creighton and D. G. Eadon, *J. Chem. Soc., Faraday Trans.*, 1991, **87**, 3881-3891.
29. R. Coppage, J. M. Slocik, B. D. Briggs, A. I. Frenkel, H. Heinz, R. R. Naik and M. R. Knecht, *J. Am. Chem. Soc.*, 2011, **133**, 12346-12349.
30. M. Newville, *Journal of Synchrotron Radiation*, 2001, **8**, 322-324.
31. R. Mais, P. Owston and A. M. Wood, *Acta Crystallographica Section B: Structural Crystallography and Crystal Chemistry*, 1972, **28**, 393-399.
32. A. Frenkel, V. S. Machavariani, A. Rubshtein, Y. Rosenberg, A. Voronel and E. Stern, *Phys. Rev. B*, 2000, **62**, 9364.
33. A. I. Frenkel, *Chem. Soc. Rev.*, 2012, **41**, 8163-8178.

34. A. I. Frenkel, Q. Wang, S. I. Sanchez, M. W. Small and R. G. Nuzzo, *J. Chem. Phys*, 2013, **138**, 064202.
35. S. Wunder, F. Polzer, Y. Lu, Y. Mei and M. Ballauff, *J. Phys. Chem. C*, 2010, **114**, 8814-8820.
36. D. Yang, R. Zhang, T. Zhao, T. Sun, X. Chu, S. Liu, E. Tang and X. Xu, *Catal. Sci. Technol.*, 2019, **9**, 6145-6151.
37. X. Chen, Z. Cai and M. Oyama, *J. Mater. Chem. A*, 2014, **2**, 5668-5674.
38. J. Kaiser, L. Leppert, H. Weilz, F. Polzer, S. Wunder, N. Wanderka, M. Albrecht, T. Lunkenbein, J. Breu, S. Kümmel, Y. Lu and M. Ballauff, *Phys. Chem. Chem. Phys.*, 2012, **14**, 6487-6495.
39. D. Wang, A. Villa, F. Porta, L. Prati and D. Su, *J. Phys. Chem. C*, 2008, **112**, 8617-8622.
40. W. Fang, Y. Deng, L. Tang, G. Zeng, Y. Zhou, X. Xie, J. Wang, Y. Wang and J. Wang, *J. Coll. Interface Sci.*, 2017, **490**, 834-843.
41. P. Fageria, S. Uppala, R. Nazir, S. Gangopadhyay, C.-H. Change, M. Basu and S. Pande, *Langmuir*, 2016, **32**, 10054-10064.
42. F. Jiang, R. Li, J. Cai, W. Xu, A. Cao, D. Chen, X. Zhang, C. Wang and C. Shu, *J. Mater. Chem. A*, 2015, **3**, 19433-19438.

FOR TABLE OF CONTENTS ONLY